Characterization and calibration of a Full Stokes polarization camera

T. Carlsen[1], A. Ehrlich[1], M. Wendisch[1]

1) Leipzig Institute for Meteorology, Leipzig University, Stephanstr. 3, 04103 Leipzig, E-Mail: tim.carlsen@uni-leipzig.de

Summary: Initially unpolarized solar radiation is polarized in the atmosphere due to scattering processes at molecules and aerosols. Therefore, the measurement of the polarization state of solar radiation is of vital importance in remote sensing. A SALSA Full Stokes polarization camera measuring the complete Stokes vectors in real time is characterized within this work. The main focus lies on the radiometric calibration as well as the determination and validation of the calibration matrix based on a Data Reduction method. One main issue is the temporal instability of the calibration matrix, which gives rise to the need of a thorough calibration process. In accordance with theoretical expectations and model simulations, the SALSA Full Stokes polarization camera provides reliable measurement results under the condition of Rayleigh scattering.

Zusammenfassung: Die beim Eintritt in die Atmosphäre unpolarisierte solare Strahlung wird durch Streuprozesse an Molekülen oder Aerosolpartikeln polarisiert. Die Messung des Polarisationszustandes der solaren Strahlung spielt deshalb in der Fernerkundung eine wichtige Rolle. Die vorliegende Arbeit charakterisiert eine SALSA Full Stokes Polarisationskamera, die den kompletten Stokes-Vektor in Echtzeit misst. Das Hauptaugenmerk liegt dabei auf der radiometrischen Kalibrierung sowie der Bestimmung und Validierung der Kalibrationsmatrix über die Methode der Datenreduktion. Die zeitliche Instabilität der Kalibrationsmatrix stellt ein großes Problem dar und stellt Anforderungen an den Umfang der Kalibrierung. Mit der SALSA Full Stokes Polarisationskamera sind zuverlässige Messungen unter einer rayleighstreuenden Atmosphäre möglich, die in Übereinstimmung mit den theoretischen Erwartungen und Modellsimulationen stehen.

1. Motivation

The radiative effect of aerosols on the climate is a major element of uncertainty in investigations of the Earth's climate change (IPCC, 2013). Therefore, the precise characterization of aerosol properties as well as the spatial extent and temporal variability of aerosol concentrations is of upmost importance. Due to its interaction with aerosols, the polarization state of solar radiation changes. Consequently, measurements of the polarization state have the ability to provide a deeper insight into aerosol

characteristics. Aerosol optical properties and their effects on climate have been investigated by either active instruments in terms of a lidar (Bösenberg and Matthias, 2003) or passive instruments in terms of sun photometers. Sun photometers measure the radiance not only in sun direction but are applied to mechanically scan the entire sky (Holben et al. 1998, Dubovik and King 2000, Bayat et al. 2013). This scanning technique is very time-consuming and requires clear-sky conditions for reliable measurements. Nevertheless, it is a suitable technique to measure aerosol properties. Imaging polarization measurements cover a wide range of observed scattering angles and are applied for atmospheric observations on satellites (Goloub et al., 2000) as well as with ground-based all-sky cameras (Kreuter and Blumthaler, 2013). The principle behind polarized all-sky imaging is based on the usage of different polarization filters that are mechanically placed into the optical path in order to measure the Stokes vector. Such imaging techniques using filters are too slow for ground-based observations during conditions with fast-moving clouds.
Since 2012, the Institute for Meteorology at Leipzig University owns a SALSA Full Stokes polarization camera made by Bossa Nova Technologies. The major advantage of this camera is the imaging technique. Due to the implemented measurement principle involving two ferroelectric liquid crystals (FLCs) and one fixed polarizer, the complete Stokes vector of the incident radiation can be measured in real time. Compared to a previous version introduced by Lefaudeux et al. (2008), the SALSA camera used here additionally measures circularly polarized components of radiation. In the following, the characterization and calibration of the polarization camera is presented.

2. Polarimetry Using the Full Stokes Polarization Camera

The SALSA polarization camera from Bossa Nova Technologies (Serial number: UOL-612-SAL-1, dimensions: 80 mm × 80 mm × 100 mm) is a passive polarimeter as it measures the radiation of an external source. It is a division-of-time polarimeter.

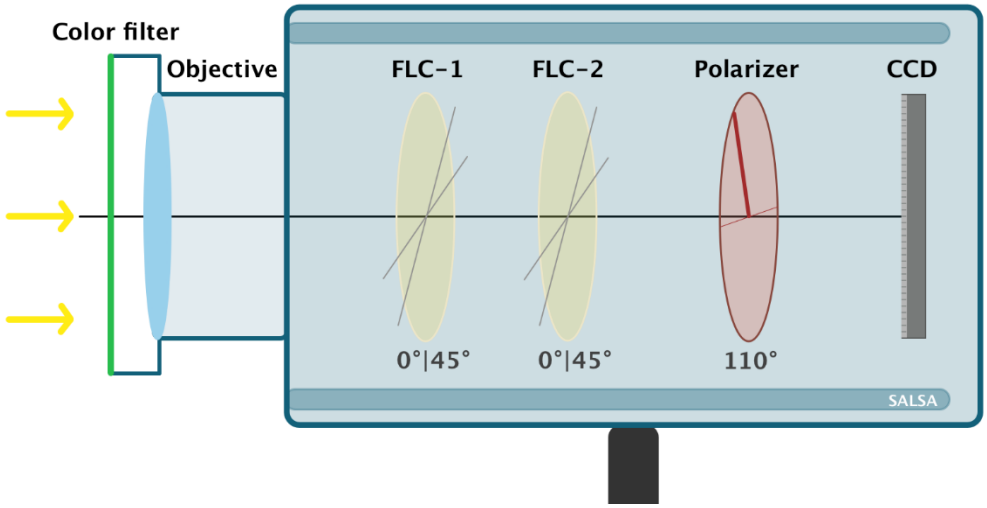

Fig. 1: Schematic set-up of the SALSA Full Stokes polarization camera

To measure the Stokes vector $\vec{S}$, 4 consecutive measurements are needed. Within the compact camera (see Fig. 1), the incident radiation initially passes through a color filter

before entering the objective (type: NMV-5M23 by Navitar, focal length: 5 mm, manual focus, iris aperture). The polarization state analyzer (PSA) consists of two FLCs and a fixed linear polarizer (transmission axis relative to horizontal: 110°). The liquid crystals each act as a programmable phase shifter, the first with a retardation close to $\lambda/2$, the second with a retardation close to $\lambda/4$. The angle of the optical axes of the FLCs with respect to the horizontal can be switched between 0 and 45 degrees. After passing the PSA, the radiation eventually reaches the CCD sensor (type: Basler avA1900-50gm, 1920×1080 pixel). During the entire work, the green color filter is used due to its higher transmission (type: HOYA G(X1) 52 mm). The intensity of the radiation I impinging on the CCD sensor can be described using the Stokes formalism as

$$\begin{aligned} I(\alpha,\theta_1,\theta_2) = \frac{1}{2}\Big\{ & S_0 + S_1\Big[\cos 2\alpha\left(\cos^2 2\theta_2 \cos 4\theta_1 + \sin 2\theta_2 \cos 2\theta_2 \sin 4\theta_1\right) \\ & + \sin 2\alpha\left(\sin 2\theta_2 \cos 2\theta_2 \cos 4\theta_1 + \sin^2 2\theta_2 \sin 4\theta_1\right)\Big] \\ & + S_2\Big[\cos 2\alpha\left(\cos^2 2\theta_2 \sin 4\theta_1 - \sin 2\theta_2 \cos 2\theta_2 \cos 4\theta_1\right) \\ & + \sin 2\alpha\left(\sin 2\theta_2 \cos 2\theta_2 \sin 4\theta_1 - \sin^2 2\theta_2 \cos 4\theta_1\right)\Big] \\ & + S_3\Big[\cos 2\alpha \sin 2\theta_2 - \cos 2\theta_2 \sin 2\alpha\Big]\Big\}, \end{aligned} \tag{1}$$

where θ_1 and θ_2 are the angles of the FLCs with respect to the x axis. α is the angle between the transmission axis of the linear polarizer and the x axis. The 4 components of the incident Stokes vector are denoted by S_i. The PSA runs through 4 different configurations for each measurement. With the known angles of the axes of the FLCs, Eq. (1) simplifies to:

$$I_1 = I(\alpha, 0°, 0°) = \frac{1}{2}\Big[S_0 + \cos 2\alpha S_1 - \sin 2\alpha S_3\Big], \tag{2a}$$

$$I_2 = I(\alpha, 45°, 0°) = \frac{1}{2}\Big[S_0 - \cos 2\alpha S_1 - \sin 2\alpha S_3\Big], \tag{2b}$$

$$I_3 = I(\alpha, 0°, 45°) = \frac{1}{2}\Big[S_0 - \sin 2\alpha S_2 + \cos 2\alpha S_3\Big], \tag{2c}$$

$$I_4 = I(\alpha, 45°, 45°) = \frac{1}{2}\Big[S_0 + \sin 2\alpha S_2 + \cos 2\alpha S_3\Big]. \tag{2d}$$

In solving this set of linear equations, the 4 unknown Stokes parameters of the incident radiation are derived:

$$S_0 = I_1 + 2I_3 - 2I_4 + I_2 + \frac{\sin 2\alpha}{\cos 2\alpha + \sin 2\alpha}\Big[I_3 - I_1 + I_4 - I_2\Big], \tag{3a}$$

$$S_1 = \frac{1}{\cos 2\alpha}\Big[I_1 - 2I_3 + 2I_4 - I_2\Big], \tag{3b}$$

$$S_2 = \frac{1}{\sin 2\alpha}\Big[I_4 - I_3\Big], \tag{3c}$$

$$S_3 = \frac{1}{\cos 2\alpha + \sin 2\alpha}\Big[I_3 - I_1 + I_4 - I_2\Big]. \tag{3d}$$

The Stokes components depend only on the 4 measured intensities. Therefore, with 4 images taken at each measurement it is possible to determine the full Stokes vector of the incident radiation.

3. General Camera Characteristics

3.1 Linearity

One great advantage of CCDs is the very linear response to the incident light intensity. In order to characterize the linearity, the radiation of an integrating sphere with variable aperture was measured. The measured intensity (corresponding to the first Stokes parameter S_0) showed a linear behaviour with respect to both the intensity of the incident radiation and the exposure time (linear correlation coefficients greater than 0.99).

3.2 Dark Current

At temperatures above absolute zero, the thermal movement of charge carriers is sufficient to excite electrons to the conduction band. Independent from any incident radiation, a certain statistically distributed dark current is measured by the CCD. The SALSA polarization camera is not cooled actively to reduce dark current. At each measurement, the dark current is subtracted immediately by means of offset maps. They consist of the dark signal measured at different gain factors at the laboratories of Bossa Nova Technologies. Several dark measurements proved the validity of this dark-frame subtraction. The CCD itself is divided into 4 separate taps. The images are therefore grabbed separately through 4 different electronic channels which allows fast image acquisition. Each tap has a different black level. Dark measurements lead to the registration of 6 digital counts for three of the 4 taps and one digital count for the fourth. This dark current is negligible compared to the maximum of 4095 counts and justifies the usage of offset maps. Furthermore, the measured dark current is independent of exposure time, gain factor and temperature (tested at $-3\ °C$ and at room temperature). Nevertheless, a similar test needs to be done for considerable higher temperatures in the future, as the exponential increase of thermally excited electrons in the conduction band might invalidate the offset maps.

3.3 Read-out Noise

Fast image acquisition can lead to a loss of electrons or an erroneous assignment of the electrons to the false pixel. Conversely, a slow read-out process poses problems due to the non-ideal insulation between different pixels. Read-out noise is independent of exposure time and measured signal. For the SALSA camera a read-out noise close to 8 digital counts was quantified.

3.4 Field of View

One main characteristic of each camera is its field of view. For achieving a sharp image on the CCD, the following trigonometric relation is valid in the internal coordinate system of the camera (CVZA: camera viewing zenith angle):

$$\mathrm{CVZA} = \arctan\frac{d}{f}\ . \tag{4}$$

Therein, the focal length of the camera is 5 mm, d denotes the distance of the image point to the center of the sensor. For the dimensions of the CCD in the SALSA camera (width: 10.56 mm, height: 5.94 mm), the field of view of the camera is

$93.12° \times 61.42° \times 100.93°$ (values corresponding to the horizontal, vertical and diagonal dimension). The maximum angular resolution is $0.046°$ per pixel.

4. Calibration of the Camera

If the polarization elements of the PSA were ideal, the Stokes parameters could be directly derived from the 4 frames at each measurement (compare Eq. (3a) to Eq. (3d)). However, due to depolarization, dispersion and manufacturing defects at the FLCs as well as the linear polarizer and polarization effects at the objective lens, the single elements do not affect incoming radiation in an ideal way. It is therefore of vital importance to determine the calibration matrix, which transfers the data of the 4 frames into the Stokes vector. The first part of this chapter deals with the implemented calibration. Furthermore, polarimetric measurements require a thorough radiometric calibration. Therefore, the second part of this chapter describes the correction of the photoresponse non-uniformity of each pixel of the sensor and the absolute calibration transferring the dimensionless signal by means of a calibration factor into the physical unit of a spectral radiance I ($\mathrm{Wm^{-2}sr^{-1}nm^{-1}}$).

4.1 Determination of the Calibration Matrix

The key factor for a correct measurement is the connection of the intensities of the 4 frames from the different configurations of the PSA with the incident, unknown Stokes vector:

$$\vec{X} = \begin{pmatrix} I_{\mathrm{frame1}} \\ I_{\mathrm{frame2}} \\ I_{\mathrm{frame3}} \\ I_{\mathrm{frame4}} \end{pmatrix} = \mathcal{C} \cdot \vec{S}_{\mathrm{in}} \ . \tag{5}$$

Matrix C is the real PSA matrix. Its inverse, C^{-1}, is the calibration matrix. The calibration matrix is determined by means of the Data Reduction Method (DRM). Each state i of the PSA is characterized by an own Mueller matrix:

$$\vec{S}^{\,i}_{\mathrm{out}} = \begin{pmatrix} S^i_{0,\mathrm{out}} \\ S^i_{1,\mathrm{out}} \\ S^i_{2,\mathrm{out}} \\ S^i_{3,\mathrm{out}} \end{pmatrix} = \begin{pmatrix} m^i_{00} & m^i_{01} & m^i_{02} & m^i_{03} \\ m^i_{10} & m^i_{11} & m^i_{12} & m^i_{13} \\ m^i_{20} & m^i_{21} & m^i_{22} & m^i_{23} \\ m^i_{30} & m^i_{31} & m^i_{32} & m^i_{33} \end{pmatrix} \vec{S}_{\mathrm{in}} \ . \tag{6}$$

As the camera sensor is insensitive to polarization, just the first row of the Mueller matrix is relevant, reducing Eq. (6) to:

$$\vec{S}^{\,i}_{0,\mathrm{out}} = m^i_{00} S_{0,\mathrm{in}} + m^i_{01} S_{1,\mathrm{in}} + m^i_{02} S_{2,\mathrm{in}} + m^i_{03} S_{3,\mathrm{in}} \ . \tag{7}$$

The aim of the calibration process is to determine the elements of the first row of the Mueller matrix for each of the 4 configurations of the PSA. For each configuration, the following system of equations in matrix form is given:

$$\begin{pmatrix} S^0_{0,\text{out}} \\ S^1_{0,\text{out}} \\ S^2_{0,\text{out}} \\ \vdots \\ S^N_{0,\text{out}} \end{pmatrix}_i = \left[\left(\vec{S}_{\text{in}}\right)^T\right] \begin{pmatrix} m^i_{00} \\ m^i_{01} \\ m^i_{02} \\ m^i_{03} \end{pmatrix} = \begin{pmatrix} S^0_{0,\text{in}} & S^0_{1,\text{in}} & S^0_{2,\text{in}} & S^0_{3,\text{in}} \\ S^1_{0,\text{in}} & S^1_{1,\text{in}} & S^1_{2,\text{in}} & S^1_{3,\text{in}} \\ S^2_{0,\text{in}} & S^2_{1,\text{in}} & S^2_{2,\text{in}} & S^2_{3,\text{in}} \\ \vdots & \vdots & \vdots & \vdots \\ S^N_{0,\text{in}} & S^N_{1,\text{in}} & S^N_{2,\text{in}} & S^N_{3,\text{in}} \end{pmatrix} \begin{pmatrix} m^i_{00} \\ m^i_{01} \\ m^i_{02} \\ m^i_{03} \end{pmatrix}, \tag{8}$$

where $\left[\left(\vec{S}_{in}\right)^T\right]$ is a $N \times 4$-matrix consisting of 4 generated Stokes parameters for each of the N measurements during the calibration process. The first row of the Mueller matrix is calculated for each state i of the PSA via:

$$\begin{pmatrix} m^i_{00} \\ m^i_{01} \\ m^i_{02} \\ m^i_{03} \end{pmatrix} = \left[\left(\vec{S}_{\text{in}}\right)^T\right]^+ \begin{pmatrix} S^0_{0,\text{out}} \\ S^1_{0,\text{out}} \\ S^2_{0,\text{out}} \\ \vdots \\ S^N_{0,\text{out}} \end{pmatrix}_i, \tag{9}$$

where $\left[\left(\vec{S}_{in}\right)^T\right]^+$ denotes the Moore-Penrose pseudoinverse of $\left[\left(\vec{S}_{in}\right)^T\right]$. The PSA matrix C consists of the first rows for each state of the PSA:

$$\vec{X} = \begin{pmatrix} I_{\text{frame1}} \\ I_{\text{frame2}} \\ I_{\text{frame3}} \\ I_{\text{frame4}} \end{pmatrix} = \mathcal{C} \cdot \vec{S}_{\text{in}} = \begin{pmatrix} m^1_{00} & m^1_{01} & m^1_{02} & m^1_{03} \\ m^2_{00} & m^2_{01} & m^2_{02} & m^2_{03} \\ m^3_{00} & m^3_{01} & m^3_{02} & m^3_{03} \\ m^4_{00} & m^4_{01} & m^4_{02} & m^4_{03} \end{pmatrix} \cdot \vec{S}_{\text{in}}\ . \tag{10}$$

Finally, the PSA matrix C is regularly inverted. This way, the calibration matrix C^{-1} (or Data Reduction Matrix) transfers the 4 measured intensities of the 4 frames into the unknown Stokes vector $\vec{S}_{in}$:

$$\vec{S}_{\text{in}} = \mathcal{C}^{-1} \begin{pmatrix} I_{\text{frame1}} \\ I_{\text{frame2}} \\ I_{\text{frame3}} \\ I_{\text{frame4}} \end{pmatrix}. \tag{11}$$

As the retardance of the individual FLCs is wavelength dependent, each color filter of the camera has its own calibration matrix. Within this work, the green wavelength channel is analyzed.

Figure 2 shows the schematic of the calibration process. An integrating sphere generates unpolarized radiation which is incident on the Polarization State Generator (PSG) consisting of a linear polarizer and a Fresnel rhomb. Both the polarizer and the Fresnel rhomb are rotatable around the propagation direction of the radiation. Within the calibration process, 1729 different polarization states were generated with the PSG and measured by the camera (lens, filter, PSA and CCD). The Fresnel rhomb was rotated

from 0° to 90° (increments of 5°). For each position of the Fresnel rhomb, the linear polarizer was rotated from 0° to 180° (increments of 2°).

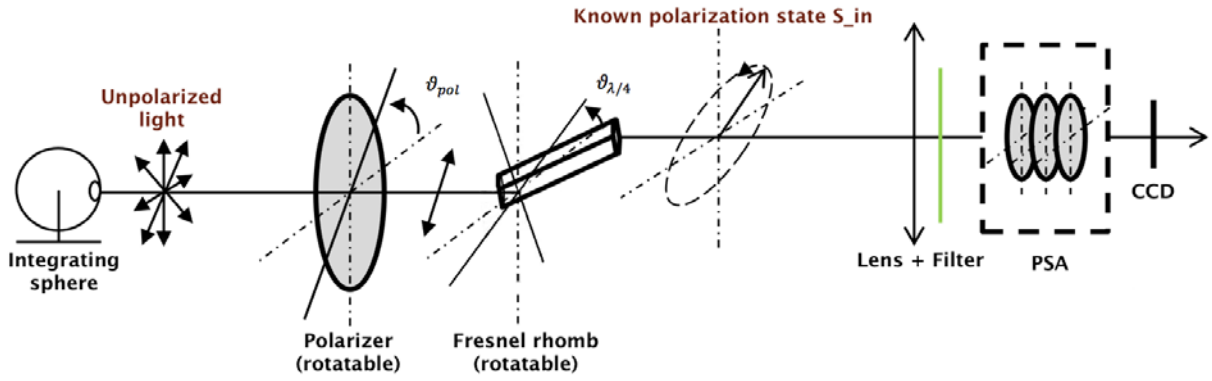

Fig. 2: Schematic of the calibration set-up (Vedel et al., 2011, modified figure 1)

The best way to visualize the generated polarization states is to use the Poincaré sphere. In a Cartesian coordinate system, the normed Stokes parameters S_1, S_2 and S_3 correspond to the x, y and z axis. For completely polarized radiation, all generated polarization states lie on the surface of a sphere with radius 1, called Poincaré sphere (see Fig. 3). All generated polarization states lie along the black paths. The dashed path visualizes the number of states on one path (one line connects two states). As illustrated in Fig. 3, the polarization states used for the calibration cover most parts of the Poincaré sphere. However, Fig. 3 also shows the view on the pole region (right part), where a huge concentration of generated polarization states is obvious. In this region, all polarization states are very similar to each other and provide just very little new information about the calibration matrix. A better coverage of the Poincaré sphere during the calibration process would allow more accurate measurements of random polarization states and should thereby be optimized during future calibrations. The calibration analyzed here still has a sufficient number of different polarization states in the equatorial region.

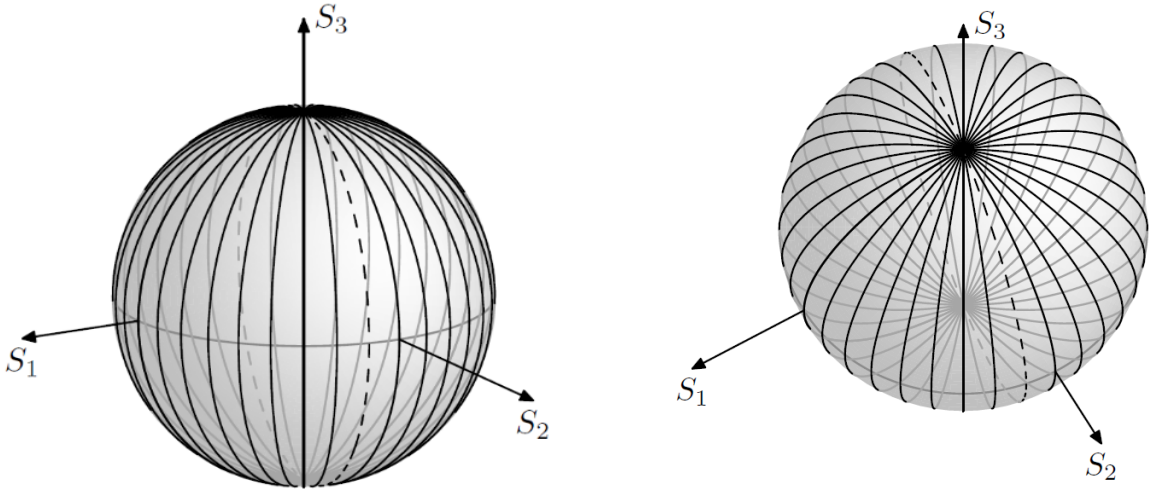

Fig. 3: Generated polarization states on Poincaré sphere (Jonsson, 2014), left: view on equator, right: view on pole

The DRM leads for 1729 generated polarization states to the calibration matrix shown in Eq. (12). For comparison, Eq. (13) shows the calibration matrix as determined in the laboratories of the manufacturer (Bossa Nova Technologies, 2012). The signs of the matrix elements in the second and third row were changed with respect to the calibration report due to a different definition of the coordinate systems.

$$\mathcal{C}^{-1} = \begin{pmatrix} 0,400021 & 0,141730 & 0,398747 & 0,059502 \\ 0,947775 & -1,226719 & 1,049670 & -0,770726 \\ 1,246871 & -0,342375 & 0,503146 & -1,407641 \\ 0,352059 & -0,175396 & -0,505731 & 0,329069 \end{pmatrix}, \tag{12}$$

$$\mathcal{C}^{-1}_{\text{BossaNova}} = \begin{pmatrix} 0,372054 & 0,171512 & 0,375346 & 0,089320 \\ 0,714034 & -1,042598 & 0,928807 & -0,587025 \\ 1,146722 & -0,257262 & 0,408144 & -1,286936 \\ 0,409610 & -0,207622 & -0,448940 & 0,249989 \end{pmatrix}. \tag{13}$$

The corresponding matrix elements of the two calibration matrices show significant deviations between 6.2 % and 33 %. This illustrates that the camera calibration has to be repeated regularly.

4.2 Radiometric Calibration

Each pixel of the CCD has its specific sensitivity due to fabrication tolerances, contamination with dust particles or optical effects at the edge of the objective lens. This photoresponse non-uniformity needs to be corrected via a radiometric calibration.

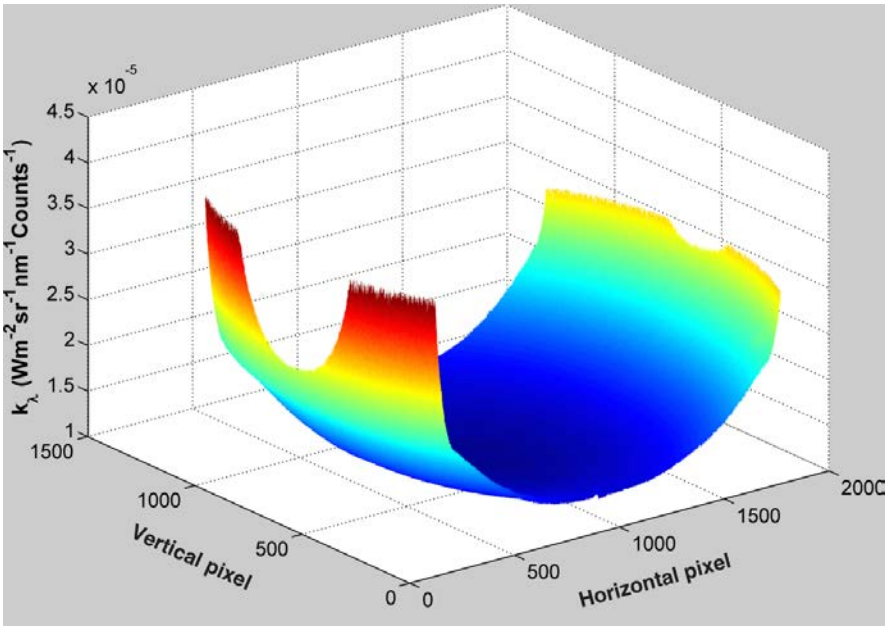

Fig. 4: Pixel-dependent illustration of the calibration factor k_λ

Therefore, the measured, uniform radiance of an integrating sphere I_λ is put in relation to the Stokes parameter S_0 determined for each pixel (x, y) by means of the calibration matrix (see Eq. (12)):

$$k_\lambda(x,y) = \frac{I_\lambda}{S_0(x,y)} \,. \tag{14}$$

The calibration factor $k_\lambda(x,y)$ corrects the different pixel sensitivities and transforms the dimensionless signal into the physical unit of a spectral radiance ($Wm^{-2}sr^{-1}nm^{-1}$). Figure 4 shows the calibration factor for an exposure time of 10 ms and gain factor 0 dB. Regions of higher sensitivity are found close to the center of the image with considerably smaller values of k_λ. This vignetting effect is typical for digital cameras and is corrected by applying the calibration factors k_λ.

5. Validation of Calibration Results

The distinct deviations of the calibration matrix elements from the manufacturer's calibration rises the need for a thorough analysis. At first, the Stokes parameters calculated by means of the calibration matrix are compared to the theoretical expectations. Secondly, temporal stability and warm-up time of the camera are investigated. The intensity of incident radiation was found to have no significant effect on the measured degree of linear polarization (DOLP).

5.1 Quality of the Calibration Matrix

Throughout the process of calibration, the theoretical Stokes vectors of the generated polarization states were already determined and can be used for the analysis. Figure 5 shows the deviations between measured and theoretical Stokes parameters S_1 for all 1729 generated polarization states.

$$\vec{S}_{\text{diff}} = \vec{S}_{\text{measured}} - \vec{S}_{\text{theoretic}} = \begin{pmatrix} \text{Dev}S_0 \\ \text{Dev}S_1 \\ \text{Dev}S_2 \\ \text{Dev}S_3 \end{pmatrix}. \tag{15}$$

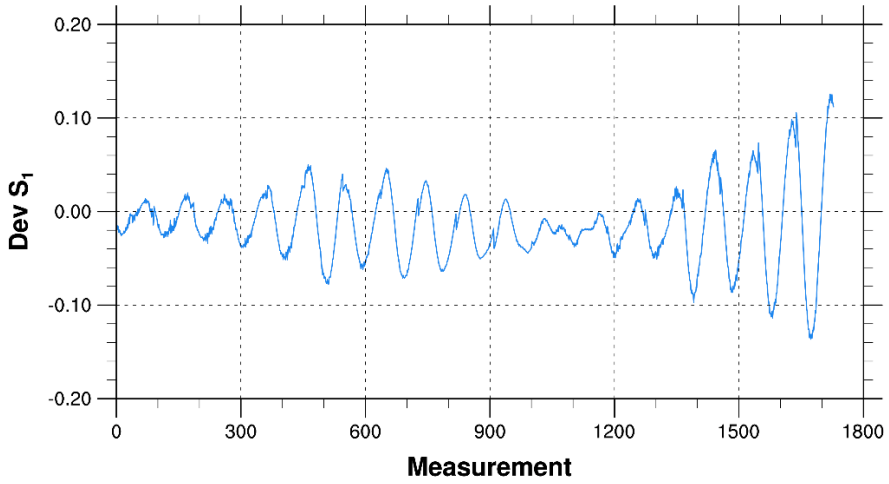

Fig. 5: Quality of the calibration matrix: standard deviation for S_1

Within Fig. 5, a pronounced periodicity of the deviations is obvious. This is due to a certain periodicity in the generated polarization states as for one position of the Fresnel

rhomb the polarizer passes through all possible positions. As the calibration matrix is the result of an error reduction, some measurements are closer to the theoretical expectations than others. The remaining Stokes parameters as well as the degree of polarization (DOP), DOLP and degree of circular polarization (DOCP) show similar behaviours (not shown here). Standard deviations can be used as a quantitative measure of the quality of the calibration matrix. Table 1 lists the standard deviations for all Stokes parameters and the different degrees of polarization when using both our calibration matrix and the manufacturer's calibration matrix. Additionally, the standard deviations as listed in the calibration report by Bossa Nova Technologies are given for comparison. Our own calibration matrix leads to maximum deviations of 5.5 % (S_2). The DOLP can be determined with deviations of ± 4.5 %. The measurement uncertainties are approximately 5-times higher than the specifications stated in the calibration report. The manufacturer's calibration matrix is based upon approximately 2000 different polarization states (15 % more than used in our calibration). Naturally, the number of generated polarization states used during the calibration has an influence on the measurement uncertainties. If just parts of the 1729 generated polarization states are used in order to determine the calibration matrix, different matrix elements are derived with different standard deviations (see Fig. 6). The higher the number of used polarization states, the more precise are subsequent measurements. Lower numbers of polarization states correspond to a worse coverage of the Poincaré sphere and lead to strongly increased uncertainties. The aim of future calibrations should therefore be to produce both a high number and preferably a sufficient variety of different polarization states in order to measure random polarization states with high precision.

Table 1: Standard deviations when using our own calibration matrix and the Bossa Nova Technologies matrix (in brackets: values from calibration report).

Standard deviation	**LIM calibration matrix**	**Bossa Nova Technologies calibration matrix**
$\sigma(S_0)$	$5.3881 \cdot 10^{-17}$	$5.1720 \cdot 10^{-17}$
$\sigma(S_1)$	0.0415	0.0942 (0.01153)
$\sigma(S_2)$	0.0547	0.0692 (0.00950)
$\sigma(S_3)$	0.0231	0.0416 (0.00630)
$\sigma(DOP)$	0.0216	0.0694
$\sigma(DOLP)$	0.0451	0.0749 (0.00923)
$\sigma(DOCP)$	0.0231	0.0416

When the Bossa Nova Technologies calibration matrix is applied to the polarization states generated in the laboratory, Stokes parameters S_1 and S_2 can only be measured with deviations of up to ± 9.4 % and ± 6.9 %, respectively (see Tab. 1). Thus, the uncertainties are one order of magnitude higher than stated in the calibration report, indicating a temporal instability of the calibration matrix. If the calibration matrix is applied to measurements which were taken three months earlier (144 different

polarization states), the measured Stokes parameters are not reliable any longer (standard deviations of up to 14 %). It cannot be ruled out that the calibration of the camera changes over time due to external influences.

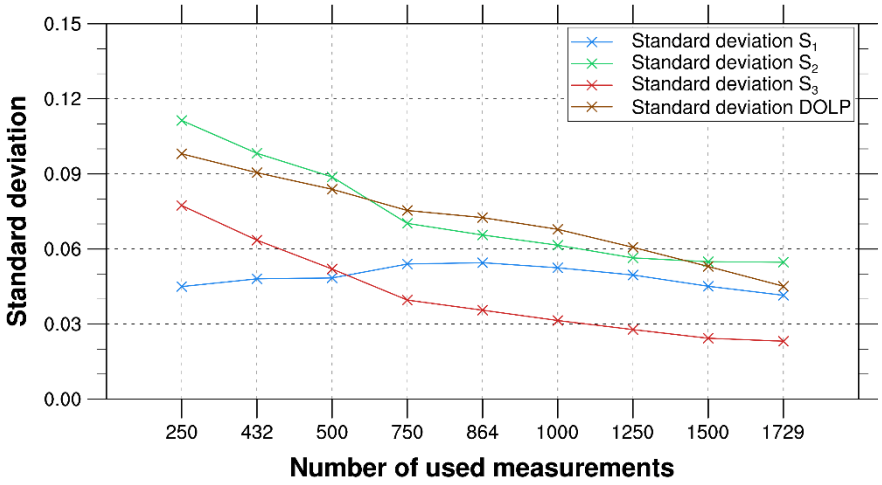

Fig. 6: Dependence of the number of used polarization states during calibration process on measurement uncertainties

5.2 Warm-up Time of the Camera

Polarized radiation ($DOLP = 1.0$) was generated by an integrating sphere and a linear polarizer (13 different positions) and measured with the camera at different times after starting the camera in order to investigate the temporal behaviour of the camera. The DOLP was measured at 13 different time steps (from 5 minutes to 4 hours after turning on the camera, see Fig. 7).

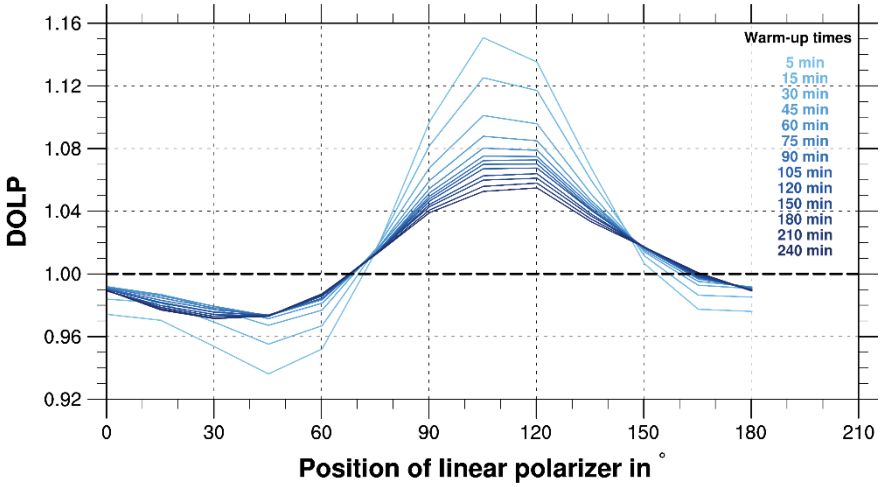

Fig. 7: Temporal evolution of DOLP measurements after camera power-on

Directly after turning on the camera, the DOLP varies between 0.94 and 1.15. Deviations of that magnitude are not acceptable for atmospheric applications of the camera. Typically, aerosol polarimetric effects are in the same order of magnitude and thus are not observable by the camera early after switching it on. However, the deviations become smaller while the camera is running. 45 minutes after power-on, the DOLP varies between 0.97 and 1.09 if the polarizer is rotated along its axis. The most precise measurements were taken after 4 hours. It should be noted that improvements became

slower with increasing runtime of the camera. Nevertheless, the camera needs a certain time after power-on in order to reach a permanent regime and measure in a reliable way. A time of 45 minutes is proposed in consideration of acceptable measurement uncertainties below 5 %.

6. Field Measurement

The sun is known to emit unpolarized radiation. Within the atmosphere, the polarization state of solar radiation changes due to numerous scattering processes. Figure 8 shows radiative transfer simulations with the MYSTIC model by Emde et al. (2010) for a molecular atmosphere. The simulated intensity shows a minimum at a viewing direction of 90° with respect to the sun. This is due to the minimum of the phase function at scattering angles of 90°. At this viewing angle, the DOP shows a pronounced maximum of approximately 65 %. On the other hand, radiation is completely unpolarized when looking into the direct sun. In order to test the camera for atmospheric applications, we performed a field measurement on 18th June 2013. The day featured a cloudless sky and therefore Rayleigh scattering conditions. Only at the end of the measurement, some altocumulus and cirrus fibratus affected the observations.

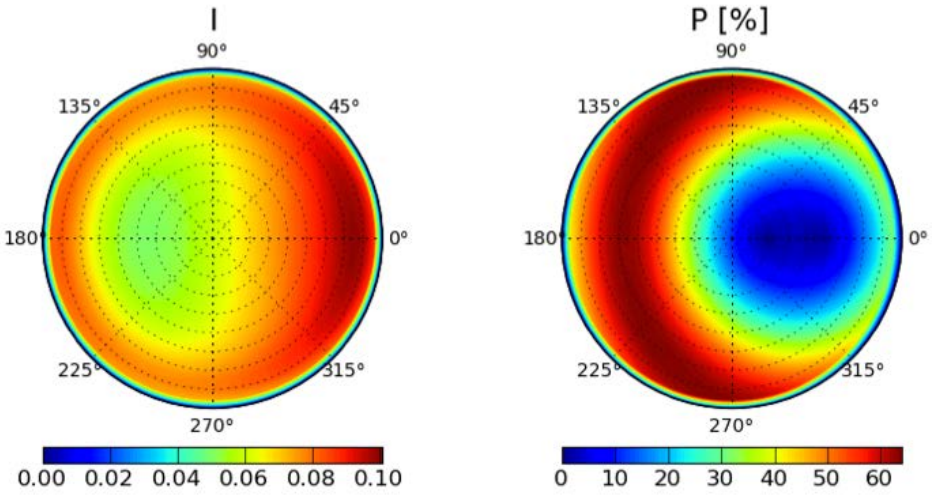

Fig. 8: Simulated intensity I and simulated degree of polarization P for molecular atmosphere (Rayleigh scattering), zenith angle: 30°, *azimuth angle:* 0°, *wavelength:* 350 *nm, surface albedo:* 0 *(Emde et al., 2010)*

The measurements were taken on the roof of the Leipzig Institute for Meteorology. The SALSA camera was mounted on a tripod and the green color filter was used. In order to cover large parts of the sky, 6 images were taken during 20 minutes starting at 2:45 p.m. (UTC). During that time, the solar zenith angle increased from 49.5° to 51.6°, the solar azimuth angle changed from 256.7° to 259.7°.

Throughout the analysis, we consecutively applied the dark current correction, the calibration matrix and the radiometric calibration to the measured signal. With help of Eq. (4) and the roll, pitch and yaw angles of the camera, each pixel of the images was related to a certain viewing angle. Afterwards, the Cartesian coordinates were transformed into polar coordinates similar to Ehrlich et al. (2012), who corrected airborne downward looking camera measurements for aircraft alignments. The

coordinate system was rotated in order to have the sun on the left side (solar azimuth angle: 270°). At pixels with more than one value from different measurements, the arithmetic mean was calculated. Figure 9 shows the polar coordinate system (all 6 images combined) and visualizes the DOLP depending on the viewing angle of the camera. The ring of high DOP values is clearly visible. The maximum DOP is 52.5 % which is smaller than the 65 % simulated by Emde et al. (2010). This can be attributed to the very idealized simulation conditions: the atmosphere was not ideally molecular due to an Aerosol Optical Depth of 0.38 at the measurement station IFT-Leipzig (AERONET, 2013) and the beginning evolution of clouds. Furthermore, the simulation was computed for a single wavelength at 350 *nm*, whereas the camera integrated over the wavelength range of the green color filter. Also, the surface albedo in reality is not zero which increases the influence of multiple scattering and decreases the DOP. A quantitative comparison is therefore not feasible. Nevertheless, a qualitative agreement between the measurements of the SALSA camera and the simulations by Emde et al. (2010) is clearly visible.

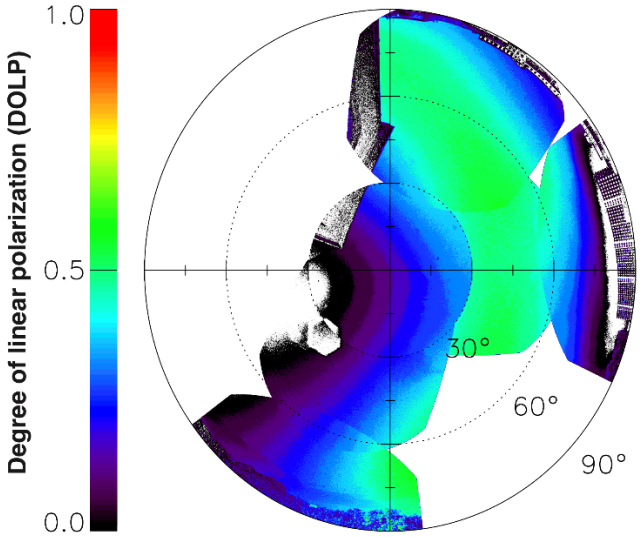

Fig. 9: Measured DOLP on 18th June 2013 in Leipzig, solar zenith angle: 50°, *solar azimuth angle:* 270°

7. Summary and Outlook

The SALSA polarization camera, a robust camera with fast image acquisition due to the use of two FLCs and a CCD with 4 separate electronic channels, was introduced and characterized by laboratory and field measurements. The SALSA polarization camera is suitable for field measurements. The qualitative agreement between the field measurement and the model simulations by Emde et al. (2010) indicates that the camera can be applied for atmospheric observations. The valid dark current correction, small read-out noise, linearity of the CCD and the independence of the intensity of incident radiation favour a high measurement accuracy. Within this work, the necessity of a thorough radiometric and polarimetric calibration became evident. One major problem is the apparent temporal instability of the calibration matrix. Already three months after

the last calibration, a measurement of the four Stokes parameters showed standard deviations of up to 14 %. Future calibrations should concentrate both on a high number and on a great variety of the generated polarization states. Furthermore, the warm-up time of the camera of about 45 minutes needs to be considered.
The findings of this work revealed sensible parts of the calibration process and allow the operation of the SALSA polarization camera in future field measurements. Future research subjects may include the derivation of aerosol properties under cloudless conditions as well as cloud detection and the retrieval of cloud properties such as effective radii.

References

AERONET, 2013: AERONET data of the station IFT-Leipzig from 18th June 2013. Aerosol Robotic Network of NASA/GSFC, Principal Investigator: Dr. Albert Ansmann, Leibniz Instititute for Tropospheric Research Leipzig.

Bayat, A., Khalesifard, H.R., Masoumi, A., 2013: Retrieval of aerosol single-scattering albedo and polarized phase function from polarized sun-photometer measurements for Zanjan's atmosphere, Atmos. Meas. Tech., 6, 2659-2669

Bösenberg, J. and Matthias, V., 2003: EARLINET: a European aerosol research lidar network to establish an aerosol climatology, MPI-Report 348, Hamburg, Germany

Bossa Nova Technologies, 2012: Calibration report – SALSA camera, Serial: UOL-612-SAL-1

Dubovik, O. and King, M., 2000: A flexible inversion algorithm for retrieval of aerosol optical properties from Sun and sky radiance measurements, Journal of Geophysical Research, 105(D16), 20673-20696

Ehrlich, A., Bierwirth, E., Wendisch, M., Herber, A., Gayet, J.-F., 2012: Airborne hyperspectral observations of surface and cloud directional reflectivity using a commercial digital camera, Atmos. Chem. Phys. 12, 3493-3510

Emde, C., Buras, R., Mayer, B., Blumthaler, M., 2010: The impact of aerosols on polarized sky radiance: model development, validation, and applications, Atmos. Chem. Phys. 10

Goloub, P., Herman, M., Chepfer, H. Riedi, J., Brogniez, G., Couvert, P., Séze, G., 2000: Cloud thermodynamical phase classification from the POLDER spaceborn instrument, Journal of Geophysical Research, 105(D11), 14747-14759

Holben, B., Eck, T.F., Slutsker, I., Tanré, D., Buis, J.P., Setzer, A., Vermote, E., Reagan, J.A., Kaufman, Y.J., Nakajima, T., Lavenu, F., Jankowiak, I., Smirnov, A., 1998: AERONET – A Federated Instrument Network and Data Archive for Aerosol Characterization, Remote Sens. Environ., 66, 1-16

IPCC, 2013: Boucher, O., Randall, D., Artaxo, P., Bretherton, C., Feingold, G., Forster, P., Kerminen, V.-M., Kondo, Y., Liao, H., Lohmann, U., Rasch, P., Satheesh, S.K., Sherwood, S., Stevens, B., Zhang, X.Y.: Clouds and Aerosols, In Climate Change 2013: The Physical Science Basis, Contribution of Working Group I to the Fifth Assessment Report of the Intergovernmental Panel on Climate Change [Stocker, T.F., Qin, D., Plattner, G.-K., Tignor, M., Allen, S.K., Boschung, J., Nauels, A., Xia, Y., Bex, V., Midgley, P.M. (eds.)], Cambridge University Press, Cambridge, United Kingdom and New York, NY, USA

Jonsson, F., 2014: C program, Visualization of Stokes parameter on Poincaré sphere, available under: http://www.jonsson.eu/programs/ansic/poincare/ (9th February 2014)

Kreuter, A. and Blumthaler, M., 2013: Feasibility of polarized all-sky imaging for aerosol characterization, Atmos. Meas. Tech., 6, 1845-1854

Lefaudeux, N., Lechocinski, N., Breugnot, S., Clemenceau, P., Bossa Nova Technologies, 2008: Compact and robust linear Stokes polarization camera, SPIE conference, Polarization: Measurement, Analysis, and Remote Sensing VIII, 6972

Vedel, M., Breugnot, S., Lechocinski, N., Bossa Nova Technologies, 2011: Full Stokes polarization camera, SPIE Proc., Vol. 8160-33, SPIE Optical Engineering + Applications